Heterogeneous dislocation loop formation near grain boundaries in a neutron-irradiated commercial FeCrAl alloy

Kevin G. Field,[1*] Samuel A. Briggs,[2] Xunxiang Hu,[3]
Yukinori Yamamoto,[4] Richard H. Howard,[5] Kumar Sridharan[6]

[1,3,4,5] Oak Ridge National Laboratory, Oak Ridge, TN 37831, USA

[2,6] University of Wisconsin–Madison, Madison, WI 53703, USA

[1] fieldkg@ornl.gov

[2] sabriggs2@wisc.edu

[3] hux1@ornl.gov

[4] yamamotoy@ornl.gov

[5] howardrh@ornl.gov

[6] kumar@engr.wisc.edu

*Corresponding author:
Kevin G. Field
Materials Science and Technology Division
PO Box 2008
Oak Ridge, TN 37831 (USA)
Phone: +1 865 241 5623
Email: fieldkg@ornl.gov

[†]*This manuscript has been authored by UT-Battelle, LLC under Contract No. DE-AC05-00OR22725 with the U.S. Department of Energy. The United States Government retains and the publisher, by accepting the article for publication, acknowledges that the United States Government retains a non-exclusive, paid-up, irrevocable, world-wide license to publish or reproduce the published form of this manuscript, or allow others to do so, for United States Government purposes. The Department of Energy will provide public access to these results of federally sponsored research in accordance with the DOE Public Access Plan (http://energy.gov/downloads/doe-public-access-plan).*

Heterogeneous dislocation loop formation near grain boundaries in a neutron-irradiated commercial FeCrAl alloy

Kevin G. Field,[1], Samuel A. Briggs,[2] Xunxiang Hu,[3]
Yukinori Yamamoto,[4] Richard H. Howard,[5] Kumar Sridharan[6]

[1,3,4,5] Oak Ridge National Laboratory, Oak Ridge, TN 37831, USA

[2,6] University of Wisconsin–Madison, Madison, WI 53703, USA

[1] fieldkg@ornl.gov

[2] sabriggs2@wisc.edu

[3] hux1@ornl.gov

[4] yamamotoy@ornl.gov

[5] howardrh@ornl.gov

[6] kumar@engr.wisc.edu

Abstract

FeCrAl alloys are an attractive class of materials for nuclear power applications because of their increased environmental compatibility compared with more traditional nuclear materials. Preliminary studies into the radiation tolerance of FeCrAl alloys under accelerated neutron testing between 300 and 400°C have shown post-irradiation microstructures containing dislocation loops and a Cr-rich α' phase. Although these initial studies established the post-irradiation microstructures, there was little to no focus on understanding the influence of pre-irradiation microstructures on this response. In this study, a well-annealed commercial FeCrAl alloy, Alkrothal 720, was neutron irradiated to 1.8 displacements per atom (dpa) at 382°C and then the effect of random high-angle grain boundaries on the spatial distribution and size of $a\langle 100\rangle$ dislocation loops, $a/2\,\langle 111\rangle$ dislocation loops, and black dot damage was analyzed using on-zone scanning transmission electron microscopy. Results showed a clear heterogeneous dislocation loop formation with $a/2\,\langle 111\rangle$ dislocation loops showing an increased number density and size, black dot damage showing a significant number density decrease, and $a\langle 100\rangle$ dislocation loops exhibiting an increased size in the vicinity of the grain boundary. These results suggest the importance of the pre-irradiation microstructure and, specifically, defect sink density spacing to the radiation tolerance of FeCrAl alloys.

Keywords: FeCrAl, Accident Tolerant, Phase Stability, Dislocation, Grain Boundary

[†] *This manuscript has been authored by UT-Battelle, LLC under Contract No. DE-AC05-00OR22725 with the U.S. Department of Energy. The United States Government retains and the publisher, by accepting the article for publication, acknowledges that the United States Government retains a non-exclusive, paid-up, irrevocable, world-wide license to publish or reproduce the published form of this manuscript, or allow others to do so, for United States Government purposes. The Department of Energy will provide public access to these results of federally sponsored research in accordance with the DOE Public Access Plan (http://energy.gov/downloads/doe-public-access-plan).*

1. Introduction

FeCrAl alloys are currently under development as a potential replacement cladding solution for zirconium-based alloys and could have other future uses in nuclear reactor applications [1]. The primary driving force for the adoption of FeCrAl alloys as a nuclear material is their generally good environmental compatibility, including high-temperature, chronic aqueous corrosion resistance and high-temperature steam oxidation resistance [2–7]. These properties lend the material the ability to perform well under both normal operation in a light water reactor (LWR) and an accident-based scenario such as a loss of coolant accident.

The radiation tolerance of FeCrAl alloys is a key issue if they are to see deployment as a nuclear-grade material. Preliminary investigations have focused on examining the compositional effect(s) on the formation of radiation-induced defect structures, including dislocation loops and radiation-enhanced precipitation of the embrittling Cr-rich α' phase [8–10]. Field et al. [8] have shown that both dislocation loop and α' phase formation can lead to radiation hardening in FeCrAl alloys, but the α' phase ultimately dominates the overall response at the dose and temperature studied. This led to further analysis by Edmondson et al. [9] and Briggs et al. [10] of α' phase formation at high temperatures and in a neutron radiation field. These works have revealed a chromium composition and damage dose effect on the precipitation of the α' phase.

However, little work has gone toward understanding the role of initial microstructure in the radiation tolerance of FeCrAl alloys. Of particular interest is the role of grain boundaries in the formation of defect and precipitate structures during irradiation. Grain boundaries have been shown to be effective defect sinks and sites for radiation-induced segregation (RIS) [11–17], precipitation-free zones [18,19], void denuded zones [20–22], helium bubble–free zones [23,24], and dislocation loop–free zones [25–30] in other material systems. Many of these observed effects can be linked to the defect-sink interactions at grain boundaries and the diffusional processes controlling the defect mobility toward the grain boundaries [31,32]. Furthermore, modification of the defect structures by the introduction of grain boundaries could have more macroscopic implications, including altering the mechanical properties of the irradiated alloy.

This work's purpose is to assess the role of high-angle grain boundaries (HAGBs) in neutron irradiation–induced defect formation in a commercial-grade FeCrAl alloy. Owing to the complexities in observing the Cr-rich α' phase using diffraction-based electron microscopy [8], dislocation loop formation was of primary interest in this work. Dislocation loop formation, as shown by Parish et al. [33], is readily observable using on-zone scanning transmission electron microscopy (STEM) –based imaging. Combining STEM-based imaging with image stitching techniques to create large fields-of-view (FOV; on the order of several microns) can provide statistically significant observations of the role of grain boundaries during sink-defect interactions in irradiated FeCrAl alloys. In this work, observations of the dislocation loop microstructure at and near grain boundaries were performed on a commercial FeCrAl alloy neutron-irradiated in the High Flux Isotope Reactor (HFIR) to 1.8 dpa at 382°C. Analysis of the heterogeneous dislocation loop formations near HAGBs also includes understanding the differences in the formation of dislocation loops with different Burgers vectors with respect to their spatial correlation to the grain boundary.

2. Materials and Methods

Alkrothal 720, a commercially available FeCrAl alloy, was used for this study. The composition was analyzed by inductively coupled plasma and combustion techniques and determined to be 12.95 wt % Cr, 4.21 wt % Al, 0.034 wt % C, 0.3 wt % Si, 0.0015 wt % S, 0.0018 wt % O, 0.0074 wt % N, and 0.008 wt % P, with a balance of Fe. Specimens for neutron irradiation in the HFIR were prepared using wire electric discharge machining to make sheet-type, dog bone–shaped SS-J2 specimens. Neutron irradiation was carried out in the HFIR to a nominal neutron fluence of 2.0×10^{25} n/m^2 (E > 0.1 MeV), resulting in a nominal damage dose of 1.8 dpa and a dose rate of 8.1×10^{-7} dpa/s. Irradiation temperature was determined using passive silicon carbide (SiC) thermometry and the standardized analysis approach/software developed by Campbell et al [34]. The irradiation temperature was estimated at 381.9 ± 5.4°C, where the error is one standard deviation of the mean from three separate SiC thermometry samples. The irradiation

capsule and hence irradiation conditions were the same as previous studies on model FeCrAl alloys with varying compositions [8,10].

For this study, one half of a broken tensile head in the neutron-irradiated state was used for electron microscopy. An as-received sample was produced in the same fashion from the original sheet product used during the tensile specimen machining. Before the focused ion beam (FIB) preparation, samples were mechanically polished using standard metallographic techniques. Electron-transparent thin foils were prepared from these polished surfaces using standardized techniques on an FEI Quanta 3D 200i FIB. All FIB-produced samples were cleaned using first a 5 kV low-energy rastered ion beam followed by a final 2 kV rastered ion beam polish. This step was crucial to reducing or, in most cases, completely eliminating any FIB-induced artifacts into the specimens.

A JEOL JEM-2100F field emission gun scanning transmission electron microscope ([S]TEM) operating at 200 kV was used for imaging dislocation loops and line dislocations. All imaging was performed using on-zone STEM imaging on the [100] zone axis by means of simultaneous bright field (BF) and annular dark field (ADF) detectors. On-zone STEM imaging enables all expected dislocation loop variants in neutron-irradiated iron-based body centered cubic (BCC) materials to be imaged in a single micrograph, greatly increasing collection efficiency while minimizing contrast interpretations [33]. For more information regarding this technique, see references [8,33,35] and the references within them. Determination of the loop type (i.e. vacancy or interstitial type) was not in the scope of this study.

Individual images were stitched together to provide both high-resolution images and a large enough FOV to enable statistically relevant analysis. Typical FOVs were 1.3×0.8 μm with the long axis orientated parallel to the grain boundary of interest. Care was taken during the stitching process to minimize any artifacts in the final image which might affect quantifications. Initially, automated software analysis of the stitched images based on Hough transform algorithms were used to determine the size and shape of each observed defect and its location with regard to the grain boundaries. Unfortunately, these algorithms were not robust enough to explicitly differentiate between edge-on $a\langle 100\rangle$ loops, tilted $a/2\,\langle 111\rangle$ loops, and in-plane $a\langle 100\rangle$ loops when the foils were imaged in the [100] orientation. Hence,

all quantification presented in this study was performed using manual counting techniques. The "fit ellipse" routine was used in ImageJ [36,37] to record each defect's spatial position (x and y), major and minor axis (i.e. diameter), and angle of the major axis to the origin of the image. Dislocation loop size was defined as the major axis of the fitted ellipse. Defect type, e.g. Burgers vector, was determined based on the morphology maps provided by Yao et al. [38] for the [100] zone axis.

An explicit source of error based on the observation and analysis technique was in the definition of the grain boundary position. To get grains orientated to the [100] zone axis, not all grain boundaries were strictly orientated edge-on to the beam. Rather, it was decided to define the grain boundary location as the center of the apparent grain boundary width. This definition limited variations in the peak zone distance and width from grain boundary to grain boundary as presented later.

After the grain boundary location was defined, using the outputs from the ellipse fitting routine, the data were input into a specialized set of algorithms to determine the quantitative information for the dislocation loop populations. To compensate for artifacts in the number density based on foil thickness, the areal density for each grain boundary was determined in 25 nm bins emanating perpendicularly from the grain boundary. Those values were then plotted as functions of their respective foil thicknesses. The slope of the areal density versus foil thickness was then used to develop an aggregate number density without foil thickness artifacts. Hence, individual number densities as a function of distance for each grain boundary are not presented here. More details on the application of this technique can be found elsewhere [39–41].

The specimen thickness for each region of interest (ROI) near a grain boundary was determined using energy-filtered transmission electron microscopy using a collection semi-angle of 6.36 mrad and assuming a normalized atomic number based on the Fe, Cr, and Al content of the alloy. Thickness maps (t_s/λ, where t_s is the specimen thickness and λ is the average inelastic scattering mean free path length-calculated to be 117.3 nm) were used, as they provided an average thickness value for the large FOV gained by the stitched STEM images. The reported error in the thickness measurement for each grain boundary represents one standard deviation of the mean used in the FOV for quantification.

Grain boundary structure was determined by indexing Kikuchi patterns generated using STEM of each adjacent grain by way of a semi-automated software program developed for TEM-based Kikuchi patterns [42]. The grain boundary misorientation angle and axis were determined from the rotation matrix between the two adjacent grains. The misorientation angle and axis were then evaluated to determine whether any low-Σ coincidence site lattice boundary criteria (Σ<15) were met [43].

3. Results

3.1 Unirradiated microstructures

The as-received microstructure had a typical ferritic equiaxed grain structure (Figure 1a) with an average grain size of 18.8±2.7 μm, measured as per ASTM E112-13 procedures [44]. STEM-based dislocation imaging revealed almost completely defect-free grains with minimal populations of line dislocation segments (Figure 1b). Dislocation line density measurements were not performed, as the density was too low to gain a statistically significant value. Limited numbers of phases, such as carbides or oxides, were observed. Based on these observations, it was determined that the prominent defect sink in the bulk samples was the grain boundary network in the sample, which is indicative of a well-annealed specimen. Note, that this is in stark contrast to the previous study of model FeCrAl alloys, which had pronounced dislocation networks in the as-received structure due to cold working [8].

3.2 Irradiated microstructures

The irradiated microstructure consisted of a high number density of resolvable dislocation loops and smaller defect clusters. No cavities were observed in any specimen. No difference in the line dislocation density was found between the unirradiated and irradiated cases. Note that small-angle neutron scattering (SANS) indicated the presence of the Cr-rich α' phase. Owing to the bulk averaging of the SANS technique, no details of the spatial distribution of the α' phase could be determined. Hence, further information on the SANS results will not be presented in this work.

A total of six grain boundaries were analyzed for heterogeneous dislocation loop formation. The basic information on the nature of these grain boundaries and their ROIs is summarized in Table 1. All grain boundaries were indexed to be random HAGBs. Random HAGBs have been shown through RIS

studies to obey the perfect sink criteria [12,15,45–48]; hence, it is anticipated that all grain boundaries will have the same or very similar defect sink strengths and interactions. Figure 2a and 2b show representative micrographs of the dislocation loop populations near one of these random HAGBs. The dislocation loops and defect clusters were determined to be $a\langle 100\rangle$ dislocation loops, $a/2\,\langle 111\rangle$ dislocation loops, and black dot damage. The indexed loop types and their respective spatial distributions and morphologies are shown in Figure 2c. Note that images in Figure 2 are a reduced FOV for graphical simplicity; total FOVs were significantly larger at 1.1×10^6 nm^2 for each grain boundary.

Figure 3 shows the calculated number density and size for the three defect types observed as a function of distance from the random HAGBs. Thickness effects were eliminated in the number density quantification by using the areal density versus thickness plot, as outlined in the materials and methods section. The quantification illustrated in Figure 3 indicates distinct trends in the heterogeneous formation of dislocation loops and defects. Near the grain boundary (<100 nm), $a/2\,\langle 111\rangle$ dislocation loops were the dominant feature, with a number density peaking at 9.7×10^{21} m^{-3} approximately 40–60 nm from the random HAGBs. The $a/2\,\langle 111\rangle$ dislocation loops were observed to be larger near the grain boundaries than in the grain interior, i.e. 18.9 ± 1.4 nm versus 8.0 ± 0.5 nm, respectively. The number density of the $a/2\,\langle 111\rangle$ dislocation loops rapidly decreased and then began to taper off with increasing distance from the grain boundary, which generally matched the size changes as a function of distance from the grain boundary.

It is interesting that the $a\langle 100\rangle$ dislocation loops did not have such a pronounced change in number density with increasing distance from the grain boundary (Figure 3b). A small peak is observed at 75–100 nm from the grain boundary, but the values tend to lie in the range of $2–3\times10^{21}$ m^{-3} regardless of distance from the grain boundary. Given this, the size variation mirrored that of the $a/2\,\langle 111\rangle$ dislocation loops as a function of distance from the grain boundaries, and the loops decreased in size with increasing distance from the grain boundary. Note that as the sizes of the $a/2\,\langle 111\rangle$ or $a\langle 100\rangle$ dislocation loops reached 9–10 nm, the resolvable limit of the on-zone STEM–based imaging technique was met, resulting

in a high proportion of defects being categorized as black dot damage. This artifact of the technique could have artificially inflated the number density values for black dot damage in Figure 3b, but it was unavoidable using this STEM-based technique.

In the grain interior, black dot damage was the most observed defect, but its number density dropped drastically as the distance to the grain boundary approached <100 nm. Its size however remained unchanged except directly adjacent to the grain boundary. Areal density–versus-thickness plots for the black dot defects typically intercepted near the origin, indicating the observed defects were not FIB-induced artifacts [39–41].

Summing all of the visible defects (dashed line in Figure 3b) shows a peak number density at ~120 nm from the grain boundary. This peak was primarily driven by the significant change (nearly an order of magnitude increase) in the black dot damage number density. Peak defect density spacing from the grain boundary has been measured in other materials and has been related to ~10× the areal defect spacing [31]. Here, the average areal defect spacing was measured as 17.3 ± 1.9 nm for the six investigated grain boundaries, resulting in a peak density distance-to-defect spacing ratio of ~7.0, a value lower than that reported for cavities in neutron-irradiated aluminum or nickel. Although not identical, the value of this ratio seems reasonable, taking into account the different material systems, defect type(s), and the fact that the defect spacing is a two-dimensional value derived from the projection of defects in a three-dimensional distribution in the FIB foil specimen.

Size distributions of all defects also changed as a function of distance from the grain boundary. Three regimes and their size distributions are shown in Figure 4. The three regimes selected are at the grain boundary (d=0–80 nm), in the transitional size and number density regime (d=100–200 nm), and in the grain interior (d>400 nm), where *d* is the distance from the grain boundary. Size distributions followed a normal or gamma distribution regardless of distance from the grain boundary. For the grain boundary regime, size distributions tended to be broad (Figure 4a). The $a/2\langle 111\rangle$ or $a\langle 100\rangle$ dislocation loops had nearly identical size distributions; hence the reported values and error shown in Figure 3a. The transitional regime and grain interior regime (Figure 4b-c) exhibit reduced full widths at half maximum

(FWHM) in the size distributions with increasing d, resulting in increasingly narrower size distributions. At the grain interior (Figure 4c), all three defect types show nearly identical size distribution widths, with only the $a/2\langle 111\rangle$ or $a\langle 100\rangle$ having a marginally higher peak size compared with the black dot damage.

4. Discussion

Neutron irradiation to 1.8 dpa at 382°C in commercial Alkrothal 720 FeCrAl induced a microstructure consistent with other high-chromium (>9 wt %) FeCr and FeCrAl alloys irradiated at similar doses and temperatures [38,49–54]. The microstructure consisted of $a/2\langle 111\rangle$ dislocation loops; $a\langle 100\rangle$ dislocation loops; black dot damage; and, although it is not discussed in detail here, the Cr-rich α' phase. A lack of cavity-induced swelling, based on the observed lack of cavities in the microstructure, was also consistent with the results for neutron-irradiated high-Cr FeCr and FeCrAl alloys irradiated to similar conditions [8,55].

The most striking result, as shown qualitatively and quantitatively in Figure 2 and Figure 3, respectively, is the stark change in the nucleation and growth of visible dislocation loops near HAGBs in the irradiated commercial-grade FeCrAl alloy. Similar results have been reported by Sakaguchi et al. [28] in a face-centered cubic (FCC) steel and Kaoumi et al. [29] in a ferritic BCC Fe-Cr steel in which loops showed denuded zones near grain boundaries. As previously noted, cavities in a wide range of irradiated metals have shown similar heterogeneous behaviors near grain boundaries [31]. Clearly, the planar sink effect of a grain boundary on heterogeneous defect accumulation and growth does not appear highly sensitive to the alloy and/or defect type. Given this, the variable magnitude of this effect in alloys with increased defect densities does indicate sensitivity to the pre-irradiation microstructure [20].

It is difficult to determine whether the observed heterogeneous dislocation loop formation near grain boundaries has any dose, temperature, and/or dose rate effect. As only one dose and temperature condition was available at the time of this study, no direct effects of these variables on the observed results can be determined. Some speculations can be offered by comparing these results with similar grain boundary effects observed in other studies. For example, denuded zones of faulted loops were found to decrease with increasing dose under elevated-temperature electron irradiation and neutron irradiation in

FCC steels [27,28]. In either case, the widths of the denuded zones were minimized when doses approached roughly 10 dpa. Temperature was also found to affect loop formation in the case of neutron-irradiated molybdenum. Brimhall and Mastel showed that, with increasing temperature, the width of a heterogeneous loop formation zone similar to the one described in this work increased [26]. The increased width of the zone with increasing temperature was attributed to the increased mobility of defects within the irradiated molybdenum specimens [26]. It is therefore probable that a dose, temperature, and/or dose rate effect exists for the grain boundary effect in neutron-irradiated FeCrAl alloys; but further studies are needed to determine the magnitude of the effect of these variables on the observed response.

The difference in the observed formation of $a/2\langle 111\rangle$ dislocation loops, $a\langle 100\rangle$ dislocation loops, and black dot damage adjacent to a random HAGB is of particular interest. This heterogeneous formation could be attributed to the mobility of these defects under elevated-temperature irradiation. Yao et al. [52] and Satoh et al. [56] showed, using in situ ion and electron irradiation, that $a/2\langle 111\rangle$ dislocation loops are mobile in the vicinity of 400°C, whereas $a\langle 100\rangle$ dislocation loops are drastically less mobile in a BCC matrix. Mobile loops produced in a region adjacent to a planar defect sink, such as a random HAGB, have a higher probability of being trapped at the defect sink. This could be the primary reason that black dot damage, which could be small $a/2\langle 111\rangle$ interstitial clusters/loops, has a decreased number density adjacent to grain boundaries compared with the hypothetically less mobile $a\langle 100\rangle$ dislocation loops. A higher mobility for black dot damage, compared with the larger and hence more stable $a/2\langle 111\rangle$ and $a\langle 100\rangle$ dislocation loops, could be the driving factor for a wider and more severe defect loss at the random HAGBs for black dots. Additionally, the absorption of point defects and small mobile defect clusters near the grain boundaries could suppress defect clustering directly adjacent to the grain boundaries, leading to decreased loop nucleation in those regions.

The increased loop sizes for both $a/2\langle 111\rangle$ dislocation loops and $a\langle 100\rangle$ dislocation loops in the vicinities of grain boundaries indicates that grain boundaries affect not only the nucleation and absorption of visible defects but also their subsequent growth. The broad size distributions for the near–grain

boundary region (d=0–80 nm) shown in Figure 4a indicate continuous growth within this region. In general, the growth of a loop can be attributed to several different phenomena, including the diffusion and absorption of point defects and small defect clusters, cascade overlap, and/or coalescence of loops [29].

Cascade overlap is least inclined to promote spatially dependent growth near the grain boundary, as cascade overlap related dislocation loop growth likely has limited impact at the elevated temperature examined here (382°C) and would be relatively insensitive to the local microstructure. Loop coalescence also has limited significance, as the largest loops are observed at ~25–50 nm from the grain boundary, but the peak defect density is 3–4× farther away than that observed distance (Figure 3). The decreased defect spacing in the peak density region would mean an increased cross-section for coalescence leading to enhanced growth, an observation not seen here.

It is most probable that the attractive force of the grain boundary for small, mobile defect clusters and the RIS of impurity atoms to the HAGB reduced the saturation of pinning defects and impurities in the region directly adjacent to the grain boundary. This under-saturation of defects and impurities promoted the diffusion of point defects in the vicinity of the grain boundary regime, resulting in an increased flux of defects to less mobile, larger loops, hence causing increased loop growth near the random HAGBs. Similarly, non–spatially dependent loop growth mechanisms have been proposed based on molecular dynamics simulations in iron in which large $a\langle 100\rangle$ dislocation loops continued to grow by biased absorption of $a/2\,\langle 111\rangle$ defect clusters [57]. Furthermore, increased interstitial mobility over vacancies and the biased sink of the grain boundaries would suggest the larger loops are interstitial in nature. Although dislocation loop nature was not investigated in this study, interstitial-type loops were identified as larger loops in the peak zone region of molybdenum after neutron irradiation at similar homologous temperatures [26].

An engineering-scale use for these findings is that the dislocation loop sizes and number densities for a given irradiation dose and temperature in irradiated FeCrAl alloys could potentially be tailored by controlling the defect density spacing of pre-irradiation defects, such as line dislocations, and the level of impurities in the base alloy. For example, cold working a material to a point at which the subgrain or

dislocation network size approaches one to two times the visible defect spacing (~120–240 nm) could lead to significantly higher bulk dislocation loop sizes and number densities. Furthermore, the ratio of $a/2\langle 111\rangle$ or $a\langle 100\rangle$ loops could be manipulated using this technique. This effect is represented in Figure 5, which compares the size and number density of dislocation loops from near-HAGB and in-grain regions in this study with the bulk size and number density of dislocation loops in a cold-worked model Fe12CrAl alloy irradiated to the same conditions [8]. The Fe12CrAl model represents a low-impurity FeCrAl alloy with grain sizes on the order of 20–30 μm, dislocation line density of $1.5 \pm 0.7\times10^{14}$ m^{-2}, and a dislocation wall spacing below 300 nm in the unirradiated state [8,58].

Figure 5 shows similar average loop sizes for the cold-worked model Fe12CrAl alloy and the near–grain boundary Alkrothal 720, indicating the high sink density in the model alloy leads to larger loops than are found in low-defect density microstructures, such as that of the in-grain well-annealed alloy studied here. Furthermore, the dominance of $a/2\langle 111\rangle$ over $a\langle 100\rangle$ loops is the same between both alloys where strong sinks were present; in regions with large defect density spacing, such as the in-grain Alkrothal 720 material studied here, $a\langle 100\rangle$ dislocation loops were found to be dominant. The higher number densities of defects in the Alkrothal 720 alloy than in the model Fe12CrAl alloy could be attributed to the higher impurity concentrations in the commercial-grade alloy; these act as trapping centers, leading to lower defect mobility under irradiation, and hence higher nucleation rates. Similar impurity effects were attributed to changes in the growth and number density of dislocation loops in Fe-9Cr and Fe-18Cr model alloys with varying levels of C, O, N, P, and Si impurities [59].

5. Conclusions

A commercial FeCrAl alloy with a nominal composition of 12.95 wt % Cr and 4.21 wt % Al was irradiated in the HFIR and then analyzed using on-zone STEM techniques to determine the role of HAGBs in dislocation loop formation during irradiation. Results showed a clear grain boundary effect with variations in the $a/2\langle 111\rangle$ dislocation loops, $a\langle 100\rangle$ dislocation loops, and black dot damage number densities and sizes as a function of distance from the grain boundary. This heterogeneous

formation on dislocation loops based on a grain boundary effect was attributed to the mobility of the defects under irradiation and the attractive forces and sink strengths of HAGBs within the low-sink-density microstructure. A comparison of the results of this study to the results of research on heavily deformed FeCrAl microstructures was presented; differences were attributed to both the observed grain boundary effect and the levels of impurities in the different alloys. Based on previously published [8] and the currently presented results and discussion, it can be concluded that not only the composition but also the pre-irradiation microstructure must be optimized to develop radiation-tolerant, nuclear-grade FeCrAl alloys.

Acknowledgments

The authors would like to thank the Irradiated Materials Examination and Testing facility and Low Activation Materials Development and Analysis laboratory staff for their continuing support of this research. Research was sponsored by the Department of Energy (DOE) Office of Nuclear Energy, Advanced Fuel Campaign of the Fuel Cycle R&D program. Neutron irradiation of FeCrAl alloys at the Oak Ridge National Laboratory's HFIR user facility was sponsored by the Scientific User Facilities Division, Office of Basic Energy Sciences, DOE. A portion of support for one of the authors (SAB) was provided by the DOE Office of Nuclear Energy University Programs.

References

[1] Y. Yamamoto, B.A. Pint, K.A. Terrani, K.G. Field, Y. Yang, L.L. Snead, Development and property evaluation of nuclear grade wrought FeCrAl fuel cladding for light water reactors, J. Nucl. Mater. 467 (2015) 703–716. doi:10.1016/j.jnucmat.2015.10.019.

[2] S.J. Zinkle, K.A. Terrani, J.C. Gehin, L.J. Ott, L.L. Snead, Accident tolerant fuels for LWRs: A perspective, J. Nucl. Mater. 448 (2014) 374–379. doi:10.1016/j.jnucmat.2013.12.005.

[3] B.A. Pint, K.A. Terrani, Y. Yamamoto, L.L. Snead, Material selection for accident tolerant fuel cladding, Metall. Mater. Trans. E. 2 (2015) 190–196.

[4] B.A. Pint, K.A. Terrani, M.P. Brady, T. Cheng, J.R. Keiser, High temperature oxidation of fuel cladding candidate materials in steam–hydrogen environments, J. Nucl. Mater. 440 (2013) 420–427. doi:10.1016/j.jnucmat.2013.05.047.

[5] B.A. Pint, K.A. Unocic, K.A. Terrani, The effect of steam on the high temperature oxidation behavior of alumina-forming alloys, Mater. High Temp. 32 (2014) 28–35.

[6] K.A. Terrani, Y.J. Kim, B.A. Pint, Uniform Corrosion of Model FeCrAl Alloys in LWR Coolants, 2015 Am. Nucl. Soc. Annu. Meet. (2015).

[7] K.A. Terrani, B.A. Pint, Y.-J. Kim, K.A. Unocic, Y. Yang, C.M. Silva, et al., Uniform corrosion of FeCrAl alloys in LWR coolant environments, J. Nucl. Mater. 479 (2016) 36–47. doi:10.1016/j.jnucmat.2016.06.047.

[8] K.G. Field, X. Hu, K.C. Littrell, Y. Yamamoto, L.L. Snead, Radiation tolerance of neutron-irradiated model Fe–Cr–Al alloys, J. Nucl. Mater. 465 (2015) 746–755. doi:10.1016/j.jnucmat.2015.06.023.

[9] P.D. Edmondson, S.A. Briggs, Y.Yamamoto, R.H. Howard, K. Sridharan, K.A. Terrani, et al., Irradiation-enhanced α′ precipitation in model FeCrAl alloys, Scr. Mater. 116 (2016) 112–116. doi:10.1016/j.scriptamat.2016.02.002.

[10] S.A. Briggs, P.D. Edmondson, Y. Yamamoto, C. Littrell, R.H. Howard, C.R. Daily, et al., A combined APT and SANS investigation of alpha prime phase precipitation in neutron-irradiated model FeCrAl alloys, Submitt. to Acta Mater. (2016).

[11] S. Watanabe, Y. Takamatsu, N. Sakaguchi, H. Takahashi, Sink effect of grain boundary on radiation-induced segregation in austenitic stainless steel, J. Nucl. Mater. 283–287 (2000) 152–156.

[12] T.S. Duh, J.J. Kai, F.R. Chen, Effects of grain boundary misorientation on solute segregation in thermally sensitized and proton-irradiated 304 stainless steel, J. Nucl. Mater. 283–287 (2000) 198–204.

[13] K.G. Field, B.D. Miller, H.J.M. Chichester, K. Sridharan, T.R. Allen, Relationship between lath boundary structure and radiation induced segregation in a neutron irradiated 9wt.% Cr model ferritic/martensitic steel, J. Nucl. Mater. 445 (2014) 143–148. doi:10.1016/j.jnucmat.2013.10.056.

[14] Y. Yang, K.G. Field, T.R. Allen, J.T. Busby, Roles of vacancy/interstitial diffusion and segregation in the microchemistry at grain boundaries of irradiated Fe–Cr–Ni alloys, J. Nucl. Mater. 473 (2016) 35–53. doi:10.1016/j.jnucmat.2016.02.007.

[15] K.G. Field, Y. Yang, T.R. Allen, J.T. Busby, Defect sink characteristics of specific grain boundary types in 304 stainless steels under high dose neutron environments, Acta Mater. 89 (2015) 438–449. doi:10.1016/j.actamat.2015.01.064.

[16] T.R. Allen, G.S. Was, Modeling radiation-induced segregation in austenitic Fe–Cr–Ni alloys, Acta Mater. 46 (1998) 3679–3691.

[17] J.P. Wharry, G.S. Was, A systematic study of radiation-induced segregation in ferritic-martensitic alloys, J. Nucl. Mater. 442 (2013) 7–16. doi:10.1016/j.jnucmat.2013.07.071.

[18] H. Jiang, R.G. Faulkner, Modelling of grain boundary segregation, precipitation and precipitate-free zones of high strength aluminium alloys—I. The model, Acta Mater. 44 (1996) 1857–1864. doi:10.1016/1359-6454(95)00317-7.

[19] T. Toyama, Y. Nozawa, W. Van Renterghem, Y. Matsukawa, M. Hatakeyama, Y. Nagai, et al., Grain boundary segregation in neutron-irradiated 304 stainless steel studied by atom probe tomography, J. Nucl. Mater. 425 (2012) 71–75. doi:10.1016/j.jnucmat.2011.11.072.

[20] A. Horsewell, B.N. Singh, Influence of Grain and Subgrain Boundaries on Void Formation and Growth in Aluminum Irradiated with Fast Neutrons, Radiation-Induced Chang. Microstruct. 13th Int. Symp. ASTM STP 9 (1987).

[21] B. Singhy, M. Eldrup, S. Zinkle, I. Golubov, On grain-size-dependent void swelling in pure copper irradiated with fission neutrons, Philos. Mag. a. 82 (2002) 1137–1159. doi:10.1080/01418610110098785.

[22] Y. Sekio, S. Yamashita, N. Sakaguchi, H. Takahashi, Void denuded zone formation for Fe–15Cr–15Ni steel and PNC316 stainless steel under neutron and electron irradiations, J. Nucl. Mater. 458 (2015) 355–360. doi:10.1016/j.jnucmat.2014.12.054.

[23] A.J.E. Foreman, B.N. Singh, Bubble nucleation in grain interior and its influence on helium accumulation at grain boundaries, J. Nucl. Mater. 133–134 (1985) 451–454. doi:10.1016/0022-3115(85)90187-4.

[24] A.I. Ryazanov, G.A. Arutyunova, V.M. Manichev, Y.N. Sokursky, V.I. Chuev, Kinetics of the growth of helium bubbles at the grain boundaries. formation of the spatially inhomogeneous distribution of helium bubbles near the grain boundaries, J. Nucl. Mater. 135 (1985) 232–245. doi:10.1016/0022-3115(85)90083-2.

[25] J.L. Brimhall, B. Mastel, T.K. Bierlein, Thermal stability of radiation produced defects in molybdenum, Acta Metall. 16 (1968).

[26] J.L. Brimhall, B. Mastel, Neutron irradiated molybdenum-relationship of microstructure to irradiation temperature, Radiat. Eff. 3 (1970) 203–215.

[27] D.J. Edwards, E.P. Simonen, S.M. Bruemmer, Evolution of fine-scale defects in stainless steels neutron-irradiated at 275 °C, J. Nucl. Mater. 317 (2003) 13–31. doi:10.1016/s0022-3115(03)00002-3.

[28] N. Sakaguchi, S. Watanabe, H. Takahashi, Heterogeneous dislocation formation and solute redistribution near grain boundaries in austenitic stainless steel under electron irradiation, Acta Mater. 49 (2001) 1129–1137. http://www.sciencedirect.com/science/article/pii/S1359645401000313.

[29] D. Kaoumi, J. Adamson, M. Kirk, Microstructure evolution of two model ferritic/martensitic steels under in situ ion irradiation at low doses (0–2 dpa), J. Nucl. Mater. 445 (2014) 12–19. doi:10.1016/j.jnucmat.2013.10.047.

[30] M. Li, M.A. Kirk, P.M. Baldo, D. Xu, B.D. Wirth, Study of defect evolution by TEM with *in situ* ion irradiation and coordinated modeling, Philos. Mag. 92 (2012) 2048–2078. doi:10.1080/14786435.2012.662601.

[31] B.N. Singh, S.J. Zinkle, Defect accumulation in pure FCC metals in the transient regime: A review, J. Nucl. Mater. 206 (1993) 212–229. doi:10.1016/0022-3115(93)90125-I.

[32] A.J. Ardell, Radiation-Induced Solute Segregation in Alloys, in: V. Ghetta, D. Gorse, D. Maziere, V. Pontikis (Eds.), Springer, 2008: pp. 285–310.

[33] C.M. Parish, K.G. Field, A.G. Certain, J.P. Wharry, Application of STEM characterization for investigating radiation effects in BCC Fe-based alloys, J. Mater. Res. 30 (2015) 1246–1274.

[34] A.A. Campbell, W.D. Porter, Y. Katoh, L.L. Snead, Method for analyzing passive silicon carbide thermometry with a continuous dilatometer to determine irradiation temperature, Nucl. Instruments Methods Phys. Res. Sect. B Beam Interact. with Mater. Atoms. 370 (2016) 49–58. doi:10.1016/j.nimb.2016.01.005.

[35] J.J. Hren, J.I. Goldstein, D.C. Joy, eds., Introduction to Analytical Electron Microscopy, Springer US, Boston, MA, 1979. doi:10.1007/978-1-4757-5581-7.

[36] M.D. Abramoff, P.J. Magalhães, S.J. Ram, Image processing with ImageJ, Biophotonics Int. 11 (2004) 36–42. http://dspace.library.uu.nl/handle/1874/204900 (accessed May 13, 2016).

[37] C.A. Schneider, W.S. Rasband, K.W. Eliceiri, NIH Image to ImageJ: 25 years of image analysis, Nat. Methods. 9 (2012) 671–675. doi:10.1038/nmeth.2089.

[38] B. Yao, D.J. Edwards, R.J. Kurtz, TEM characterization of dislocation loops in irradiated BCC Fe-based steels, J. Nucl. Mater. 434 (2013) 402–410. doi:10.1016/j.jnucmat.2012.12.002.

[39] S.J. Zinkle, Y. Matsukawa, Observation and analysis of defect cluster production and interactions with dislocations, J. Nucl. Mater. 329–333 (2004) 88–96. doi:10.1016/j.jnucmat.2004.04.298.

[40] N. Yoshida, M. Kiritani, F.E. Fujita, Electron radiation damage of iron in high voltage electron microscope, J. Phys. Soc. Japan. 39 (1975) 170–179.

[41] S. Kojima, S. Zinkle, Radiation hardening in neutron-irradiated polycrystalline copper: Barrier strength of defect clusters, J. Nucl. Mater. 179–181 (1991) 982–985.

[42] J.-J. Fundenberger, A. Morawiec, E. Bouzy, J.S. Lecomte, Polycrystal orientation maps from TEM, Ultramicroscopy. 96 (2003) 127–137.

[43] D.G. Brandon, The structure of high-angle grain boundaries, Acta Metall. 14 (1966) 1479–1484.

[44] ASTM, Standard Test Methods for Determining Average Grain Size, E112-12. (2012). doi:10.1520/e0112-12.

[45] R. Hu, G.D.W. Smith, E.A. Marquis, Effect of grain boundary orientation on radiation-induced segregation in a Fe–15.2 at.% Cr alloy, Acta Mater. 61 (2013) 3490–3498. doi:10.1016/j.actamat.2013.02.043.

[46] K.G. Field, L.M. Barnard, C.M. Parish, J.T. Busby, D. Morgan, T.R. Allen, Dependence on grain boundary structure of radiation induced segregation in a 9 wt % Cr model ferritic/martensitic steel, J. Nucl. Mater. 435 (2013) 172–180. doi:10.1016/j.jnucmat.2012.12.026.

[47] T.S. Duh, J.J. Kai, F.R. Chen, L.H. Wang, Numerical simulation modeling on the effects of grain boundary misorientation on radiation-induced solute segregation in 304 austenitic stainless steels, J. Nucl. Mater. 294 (2001) 267–273.

[48] W.Z. Han, M.J. Demkowicz, E.G. Fu, Y.Q. Wang, A. Misra, Effect of grain boundary character on sink efficiency, Acta Mater. 60 (2012) 6341–6351. doi:10.1016/j.actamat.2012.08.009.

[49] J. Chen, P. Jung, W. Hoffelner, H. Ullmaier, Dislocation loops and bubbles in oxide dispersion strengthened ferritic steel after helium implantation under stress, Acta Mater. 56 (2008) 250–258. doi:10.1016/j.actamat.2007.09.016.

[50] M. Matijasevic, E. Lucon, A. Almazouzi, Behavior of ferritic/martensitic steels after n-irradiation at 200 and 300°C, J. Nucl. Mater. 377 (2008) 101–108. doi:10.1016/j.jnucmat.2008.02.063.

[51] S.I. Porollo, A.M. Dvoriashin, A.N. Vorobyev, Y. V Konobeev, The microstructure and tensile properties of Fe-Cr alloys after neutron irradiation at 400°C to 5.5–7.1 dpa, J. Nucl. Mater. 256 (1998) 247–253.

[52] Z. Yao, M. Hernández-Mayoral, M.L. Jenkins, M.A. Kirk, Heavy-ion irradiations of Fe and Fe–Cr model alloys Part 1: Damage evolution in thin-foils at lower doses, Philos. Mag. 88 (2008) 2851–2880. doi:10.1080/14786430802380469.

[53] D. Gelles, Microstructural examination of neutron-irradiated simple ferritic alloys, J. Nucl. Mater. 108 & 109 (1982) 515–526.

[54] Y. Katoh, A. Kohyama, D. Gelles, Swelling and dislocation evolution in simple ferritic alloys irradiated to high fluence in FFTF/MOTA, J. Nucl. Mater. 225 (1995) 154–162.

[55] E.A. Little, D.A. Stow, Void-swelling in irons and ferritic steels, J. Nucl. Mater. 87 (1979) 25–39.

[56] Y. Satoh, H. Matsui, T. Hamaoka, Effects of impurities on one-dimensional migration of interstitial clusters in iron under electron irradiation, (n.d.). doi:10.1103/PhysRevB.77.094135.

[57] J. Marian, B.D. Wirth, R. Schaublin, G.R. Odette, J.M. Perlado, MD modeling of defects in Fe and their interactions, J. Nucl. Mater. 323 (2003) 181–191. doi:10.1016/j.jnucmat.2003.08.037.

[58] K.G. Field, S.A. Briggs, P.D. Edmondson, J.C. Haley, R.H. Howard, X. Hu, et al., Database on Performance of Neutron Irradiated FeCrAl Alloys, Oak Ridge, TN, 2016.

[59] E. Wakai, A. Hishinuma, Y. Kato, H. Yano, S. Takaki, K. Abiko, (JAERI, Tokai), Radiation induced alpha-prime phase formation on dislocation loops in Fe-Cr alloys during electron irradiation, J. Phys. IV. 5 (1995) C7–277 – C7–286. doi:10.1051/jp4:1995733.

Tables

Table 1: Summary of grain boundaries that were analyzed for heterogeneous formation of dislocation loops after neutron irradiation.

Boundary ID	Property			
	Mis. angle(°)/axis	GB-type	Specimen Thickness (nm)	Number Defects Counted
1	39.3 [$\bar{3}\bar{2}\bar{2}$]	RHAGB	87.1 ± 6.4	1833
2	52.2 [$\bar{3}02$]	RHAGB	74.5 ± 5.2	1609
3	36.0 [102]	RHAGB	81.9 ± 8.1	1179
4	34.5 [$2\bar{1}4$]	RHAGB	63.7 ± 4.1	1023
5	46.8 [103]	RHAGB	73.7 ± 6.9	1177
6	40.8 [$0\bar{1}3$]	RHAGB	96.3 ± 7.8	1569

RHAGB = random high-angle grain boundary.

Figures

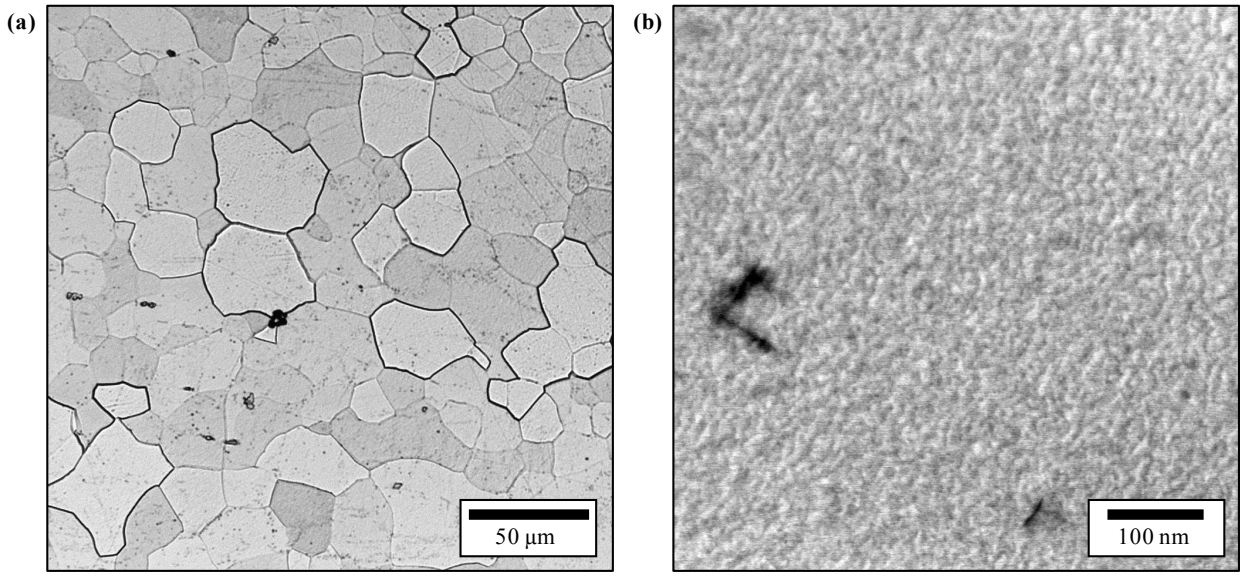

Figure 1: As-received microstructure of the Alkrothal 720 FeCrAl alloy. (a) Optical micrograph showing the ferritic grain structure, (b) BF-STEM image showing minimal line dislocation networking (black contrast).

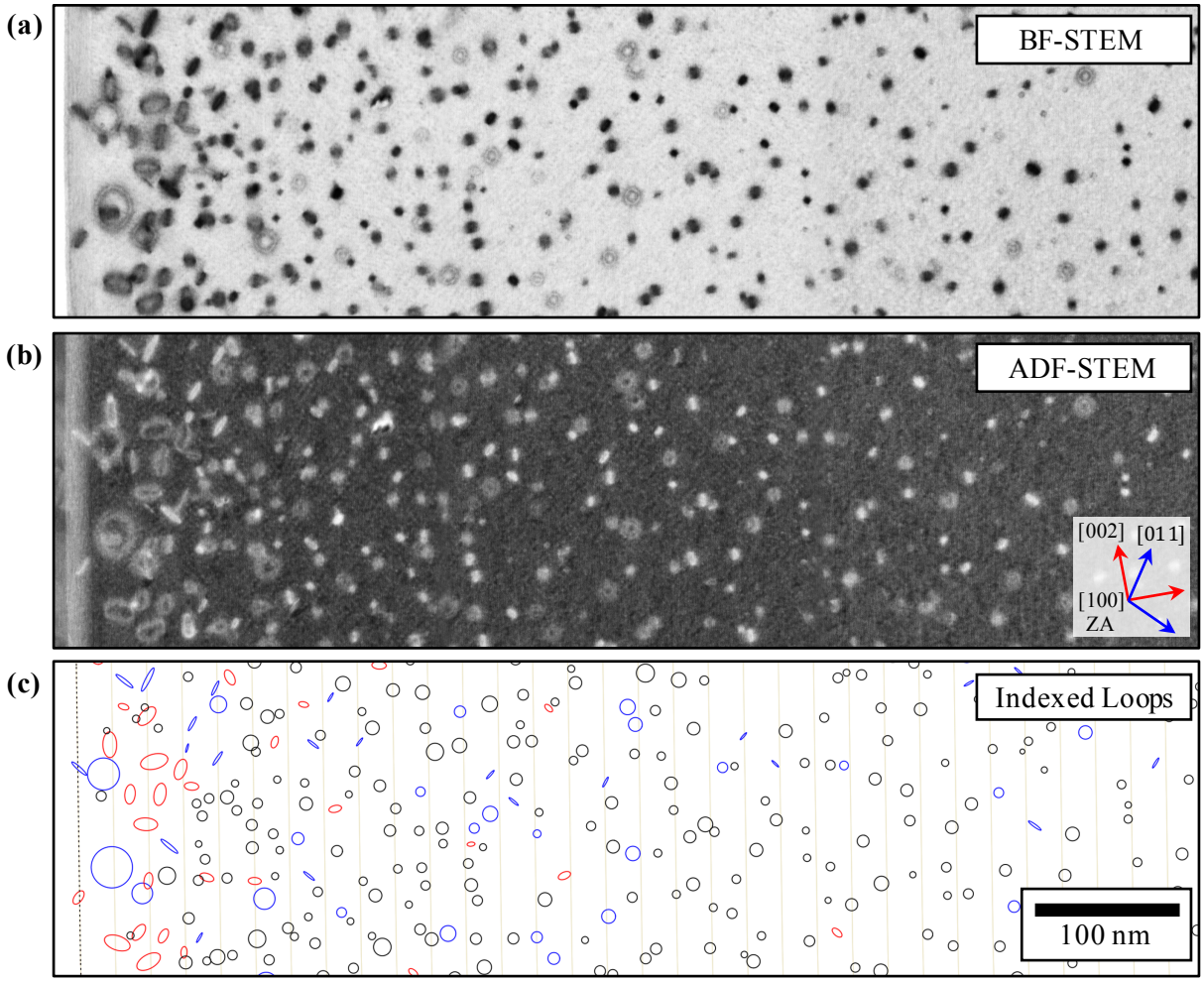

Figure 2: Dislocation loop distribution as a function of distance from the grain boundary (band on left in images) after neutron irradiation to 1.8 dpa at 382°C from grain boundary 2 in Table 1. (a) BF-STEM image, (b) ADF-STEM image, (c) indexed loop map showing different loop types: black circles are black dot damage, red ellipses are $a/2\langle 111\rangle$ loops, blue circles are in-plane $a\langle 100\rangle$ loops, and blue ellipses are edge-on $a\langle 100\rangle$ loops. Thickness of sample is 74.5±5.2 nm.

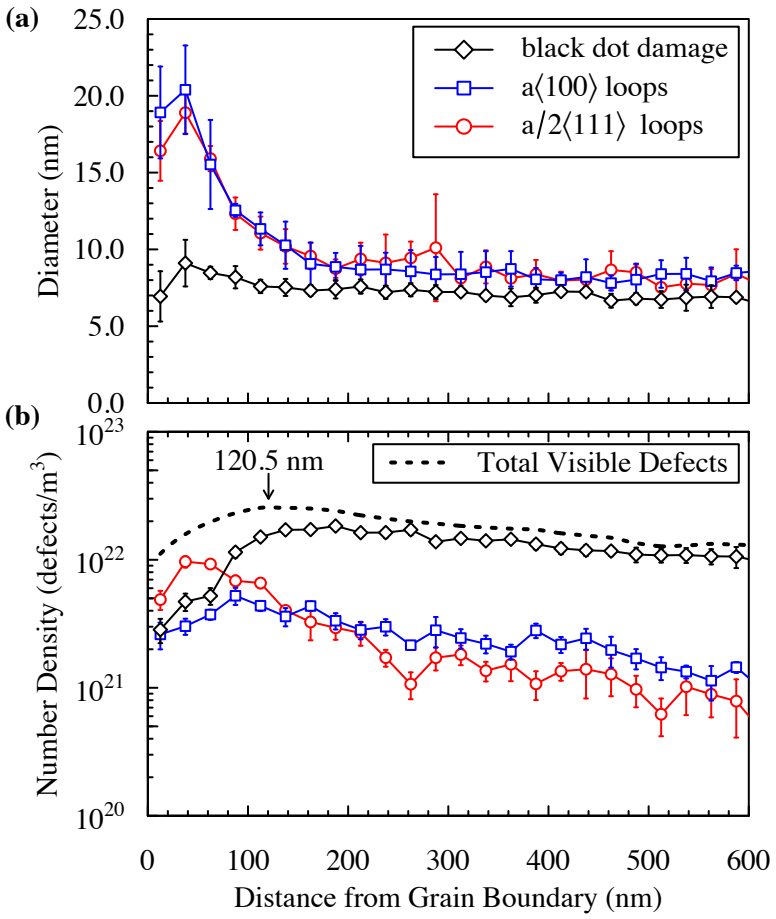

Figure 3: Size and number density of observed defects after neutron irradiation to 1.8 dpa at 382°C as a function of distance from the grain boundary based on aggregate values from all grain boundaries. Error bars in (a) denote one standard deviation of the mean of all grain boundaries; error bars in (b) are generated from the standard error of the linear regression to compensate for foil thickness variations.

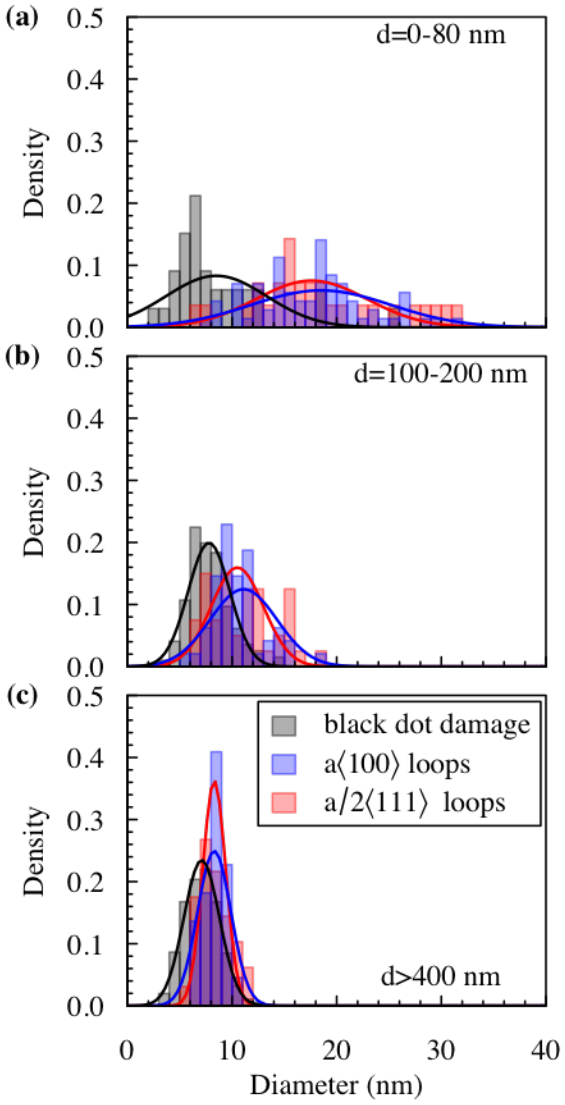

Figure 4: Size distributions of black dot damage, $a\langle 100\rangle$, and $a/2\,\langle 111\rangle$ after neutron irradiation to 1.8 dpa at 382°C from grain boundary 3 in Table 1 where "d" in the figures denotes the range of distance from the grain boundary: (a) the near–grain boundary region, (b) the transitional region, (c) the grain interior region.

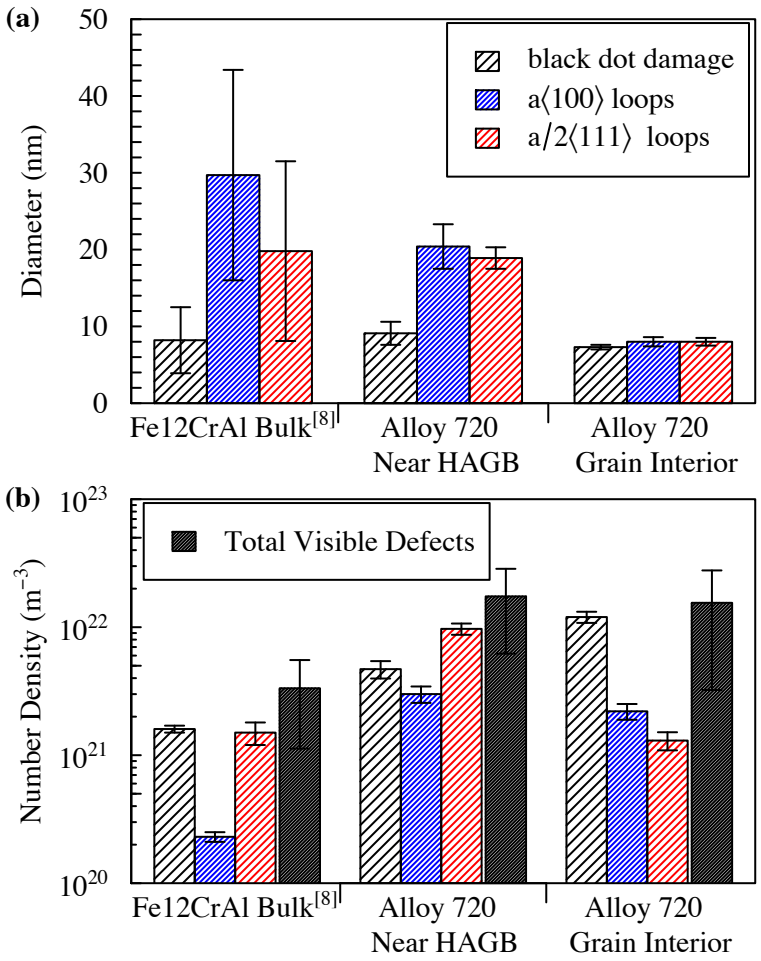

Figure 5: Comparison of size and number densities of imaged defects after neutron irradiation to 1.8 dpa at 382°C in a cold-worked model Fe12CrAl alloy from Field et al. [8] with the defects observed in this study near the HAGBs and from the grain interior.